Thermally enhanced mechanical properties of arc evaporated $Ti_{0.34}Al_{0.66}N$/TiN multilayer coatings

Axel Knutsson, Magnus P Johansson, L Karlsson and Magnus Odén

Original Publication:

Axel Knutsson, Magnus P Johansson, L Karlsson and Magnus Odén, Thermally enhanced mechanical properties of arc evaporated $Ti_{0.34}Al_{0.66}N$/TiN multilayer coatings, 2010, JOURNAL OF APPLIED PHYSICS, (108), 4, 044312.
http://dx.doi.org/10.1063/1.3463422

Thermally enhanced mechanical properties of arc evaporated $Ti_{0.34}Al_{0.66}N/TiN$ multilayer coatings

A. Knutsson,[1,a)] M. P. Johansson,[1,2] L. Karlsson,[2] and M. Odén[1]
[1]*Nanostructured Materials Division, Department of Physics, Chemistry and Biology, IFM, Linköping University, SE-58183 Linköping, Sweden*
[2]*Seco Tools AB, SE-73782 Fagersta, Sweden*

(Received 11 March 2010; accepted 15 June 2010; published online 23 August 2010)

Cubic metastable $Ti_{0.34}Al_{0.66}N/TiN$ multilayer coatings of three different periods, 25+50, 12+25, and 6+12 nm, and monoliths of $Ti_{0.34}Al_{0.66}N$ and TiN where grown by reactive arc evaporation. Differential scanning calorimetry reveals that the isostructural spinodal decomposition to AlN and TiN in the multilayers starts at a lower temperature compared to the monolithic TiAlN, while the subsequent transformation from *c*-AlN to *h*-AlN is delayed to higher temperatures. Mechanical testing by nanoindentation reveals that, despite the 60 vol % TiN, the as-deposited multilayers show similar or slightly higher hardness than the monolithic $Ti_{0.34}Al_{0.66}N$. In addition, the multilayers show a more pronounced age hardening compared to the monolith. The enhanced hardening phenomena and improved thermal stability of the multilayer coatings are discussed in terms of particle confinement and coherency stresses from the neighboring TiN-layers. © *2010 American Institute of Physics*. [doi:10.1063/1.3463422]

I. INTRODUCTION

Protective $Ti_{1-x}Al_xN$ physical vapor deposition (PVD) coatings have been used in the cutting tool industry since 1990s.[1,2] Previous studies[3,4] have shown improved thermal stability in terms of mechanical properties of cathodic arc evaporated supersaturated solid solution coatings of cubic (*c*) $Ti_{1-x}Al_xN$ compared to binaries, e.g., TiN and CrN.[5] The observed age hardening, i.e., increase in the hardness upon postannealing, is associated with an isostructural phase separation into coherent nanometer-sized *c*-TiN and *c*-AlN rich precipitates at elevated temperature.[6] These precipitates grow and coalesce upon further annealing until *c*-AlN transforms to hexagonal (*h*) AlN and the coherency is lost accompanied with a deterioration of the mechanical properties.[7] It has been suggested that the phase separation is a spinodal decomposition since *ab initio* calculations predict a miscibility gap for the cubic B1 $Ti_{1-x}Al_xN$ solid solution.[8,9] Hence, in order to further enhance the high temperature properties, the *c*-AlN to *h*-AlN transformation needs to be suppressed. Here we have attempted to achieve this by limiting the growth of the *c*-AlN precipitates by introducing 12–50-nm-thick TiN-layers in a nanolaminated $Ti_{1-x}Al_xN/TiN$ coating structure. The idea is to utilize the fact that TiN and AlN are immiscible but still has a lattice mismatch small enough to allow coherency. The drawback with such approach is the introduction of a component, TiN, which has substantially lower high temperature mechanical properties and overall lower hardness. On the other hand, multilayer/laminated coating structures have proven to exhibit hardening[10] due to shear modulus differences between the layers[11] and coherency strain at the internal interfaces.[12] The introduction of nanometer-thick sublayers results in a Hall–Petch type[13,14] strengthening of the multilayer where the hardness increases due dislocation pile-ups at the internal interfaces. Thus, multilayer hardening could compensate for the poor high temperature properties of TiN.

In this paper we report on age hardening and the kinetics of thermal decomposition of $Ti_{0.34}Al_{0.66}N/TiN$ multilayers and how these phenomena are affected by the multilayer architecture, i.e., the size of transforming material. We have used differential scanning calorimetery to study the decomposition, x-ray diffractometry, high resolution transmission electron microcopy and analytical scanning transmission electron microscopy for microstructure characterization, and nanoindententation for mechanical property determination.

II. EXPERIMENTAL DETAILS

Coatings were deposited using a commercial Sulzer/Metaplas MZR-323 reactive cathodic arc evaporation system in a N_2 atmosphere of 2 Pa, a base pressure of 0.5 mPa, bias of −55 V, and substrate temperature of 400 °C. Three circular 63 mm cathodes of $Ti_{0.34}Al_{0.66}$ were mounted facing three cathodes of Ti. Cleaned cemented carbide substrates [Seco Tools "HX," chemical composition (wt %) WC 94—Co6] polished to a mirror like surface finish and Fe foils was mounted on a one axis rotating drum, see Fig. 1. An intentionally displacement in height of the two different types of cathodes resulted in passages of the substrates through the region of maximum deposition rate for the Ti cathodes and through a region with lower deposition rate for the $Ti_{0.33}Al_{0.67}$ cathodes, resulting in a nonsymmetric multilayer of alternating $Ti_{0.34}Al_{0.66}N$ and TiN-layers to a total thickness of 2 μm. The drum was set to rotate 1 rpm, 2 rpm, and 4 rpm which resulted in three different layer periods, Λ, of 25+50 nm, 12+25 nm, and 6+12 nm, respectively. 2 μm thick monolithic TiN and $Ti_{0.34}Al_{0.66}N$ coatings, deposited under identical conditions as the multilayers, where used as reference coatings.

a)Electronic mail: knutsson@ifm.liu.se.

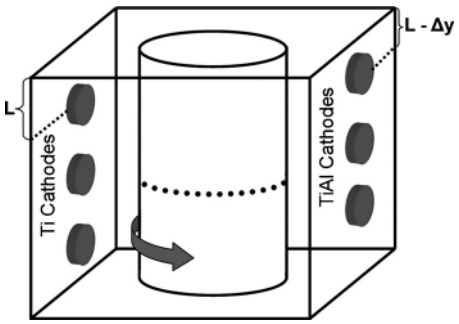

FIG. 1. Schematics of the deposition system. Dotted line on the drum indicates substrate position, L the position of the Ti Cathodes and Δy the shift in the TiAl cathodes relative to the Ti cathodes.

Isothermal postannealing at 800, 900, 950, 1000, 1050, and 1100 °C were carried out in a protective argon atmosphere at ambient pressure in a Sintervac Furnace from GCA Vacuum Industries. The heating rate was 7 °C/min until 40 °C below maximum temperature, T_{max}, where it was decreased to 5 °C/min. After 2 h annealing at T_{max} samples were cooled to 500 °C in ~1.5 h and from 500 to 100 °C in ~4 h.

X-ray diffraction (XRD) measurements were performed using a Bruker AXS D8-advanced x-ray diffractometer equipped with a Cu K_α x-ray source and operated in line focus. $\theta-2\theta$ scans were performed from 20° to 80° in the 2θ range.

A Fei Tecnai G^2 TF 20 UT microscope operating at 200 kV and equipped with an energy dispersive x-ray spectrometer (EDX) was used for transmission electron microscopy (TEM), scanning TEM (STEM), and EDX mapping. STEM analysis was performed with a high angle annular dark field detector with a camera length of 220 mm. Cross sectional TEM/STEM samples of the coating deposited on WC–Co substrates were prepared by mechanical grinding and polishing followed by Ar-ion beam milling to electron transparency.

The hardness measurements were performed with an UMIS nanoindentor equipped with a Berkovich diamond tip. Because of the roughness of arc evaporated thin films, the tapered cross sectional samples (taper angle ≈10°) were prepared through mechanical grinding and polishing. The final polishing step, 1 μm diamond paste, resulted in a mirror like surface finish. The samples were demagnetized and cleaned with ethanol before mounted in the nanoindenter. Approximately 30 indents were performed in each sample. Hardness values were extracted from the load-displacement curves using the method developed by Oliver and Pharr[15] and the average hardness number and its standard deviation is reported here. A fused silica reference was used to check calibrations between every sample.

A Netsch STA 410 differential scanning calorimeter (DSC) was used for thermal analysis. Samples were prepared by dissolving the Fe foil substrates in 64% hydrochloric acid for 48 h and collect the as-deposited coating, now in the shape of mm sized flakes. The washed and dried flakes was ground to a fine powder and compacted into an Al_2O_3 crucible. Approximately 50 mg of powder was used for each anneal and before starting the heat treatment the sample was out-gassed for 12 h at 250 °C and 0.5 mPa. A run consisted of heating the samples to the maximum temperature 1450 °C with a constant heating rate of 20 °C/min directly followed by cooling to room temperature (RT). Directly after the first heating/cooling cycle an identical cycle was performed, which was used for the baseline correction. All DSC measurements were performed in a 50 ml/min protective He flow.

III. RESULTS

The color of the as-deposited multilayer coatings change from blue-purple to cupper-brown for the 1 rpm and 4 rpm, respectively. Postdeposition annealing did not result in any color change except for a slight darkening.

A. Microstructural changes due to heat treatments

Figure 2(a) shows x-ray diffractograms from monolithic $Ti_{0.34}Al_{0.66}N$ on WC–Co substrate in its as-deposited state and heat treated at 900, 1000, and 1100 °C. The only diffraction peaks observed in the as-deposited state, except for the substrate peaks, originate from face center cubic (fcc) $Ti_{0.34}Al_{0.66}N$ at 37.48°2θ (111) and 43.50°2θ (200). The diffractogram from the coating heat treated at 900 °C shows a decrease in the diffraction peak intensities from fcc-$Ti_{0.34}Al_{0.66}N$ and the appearance of fcc-TiN at 42.65°2θ (200) and fcc-AlN at 43.95°2θ (200). Heat treatment at 1000 °C resulted in a decrease in the *c*-AlN peak intensity and the appearance of a (1010) *h*-AlN peak at 33.23°2θ. After heat treatments at 1100 °C no change in the *h*-AlN intensity is seen. In addition, diffraction peaks corresponding to Co exist in the diffractograms from coatings heat treated at 1000 and 1100 °C. The migration of Co from the substrate into the coating is known phenomenon in this system.[3]

Figure 2(b)–2(d) shows x-ray diffractograms from multilayers deposited with 1 rpm, 2 rpm, and 4 rpm drum rotation, respectively, in their as-deposited state and heat treated at 900, 1000, and 1100 °C. The 1 rpm multilayer in the as-deposited state shows peaks corresponding to the $Ti_{0.34}Al_{0.66}N$ (111) and (200) at 37.43°2θ and 43.56°2θ respectively. Also clear peaks from the TiN (111) and (200) are observed at 36.42°2θ and 42.55°2θ respectively. After heat treatment at 900 °C the TiN peaks increase and the $Ti_{0.34}Al_{0.66}N$ peaks decrease. The diffractogram now also shows signs of peaks corresponding to the *c*-AlN (111) and (200) positioned at 37.78°2θ and 44.20°2θ, respectively. Heat treatments at 1000 °C result in a decrease in the (200) *c*-AlN peak and increase in all the TiN and the (1010) *h*-AlN peaks. Heat treatments at 1100 °C only result in further increase in the (1010) *h*-AlN peak intensity. The diffractogram from the 2 rpm multilayer in its as-deposited state, Fig. 2(c), shows TiN and $Ti_{0.34}Al_{0.66}N$ peaks similar to what was seen for the multilayer deposited with 1 rpm. Heat treatments at 900, 1000 and 1100 °C of the 2 rpm multilayer result in the same peak evolution as in the diffractograms of the 1 rpm multilayer. The diffractograms from the 4 rpm multilayer in as-deposited state Fig. 2(d) show a superlattice (SL) peak, SL at 42.81°2θ with resulting SL satellites, SL−1 and SL

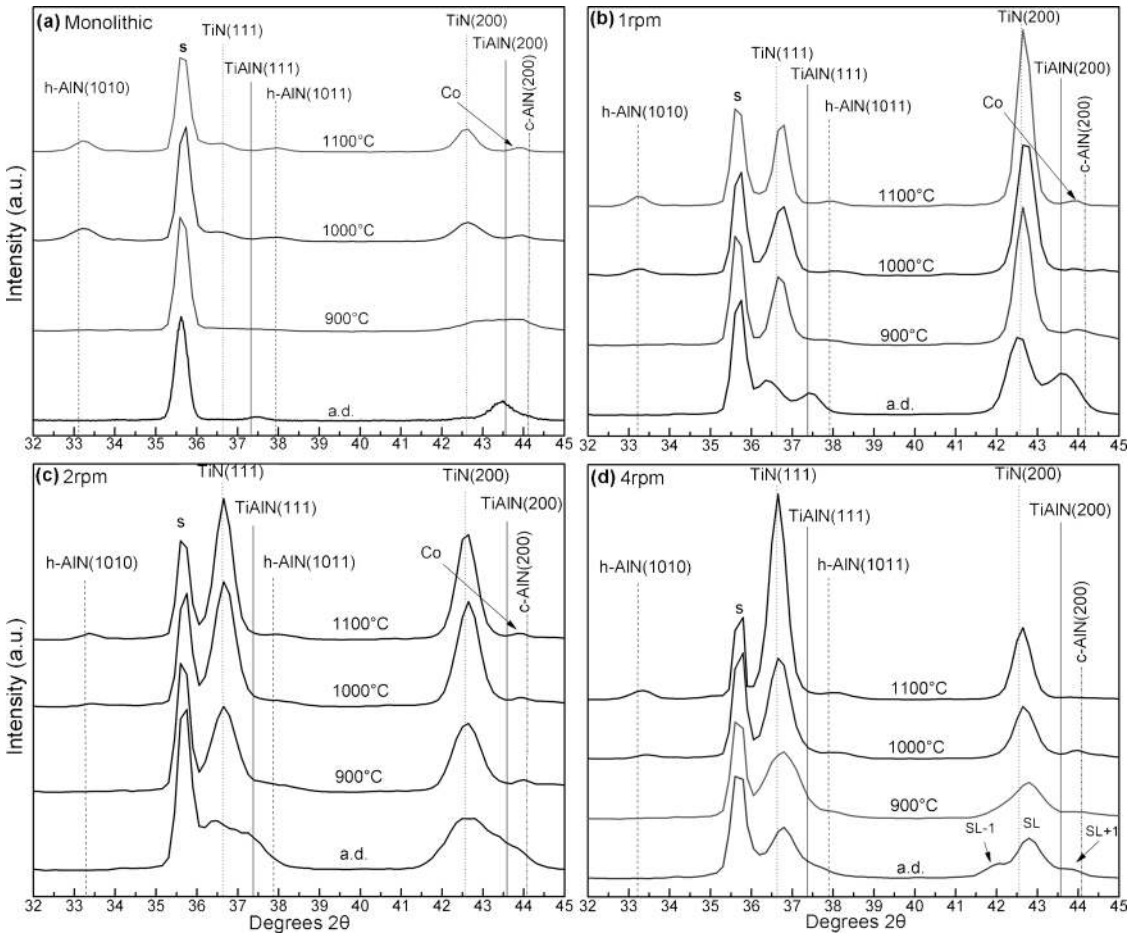

FIG. 2. X-ray diffractograms of as-deposited and heat treated (a) monolithic $Ti_{0.34}Al_{0.66}N$ and $Ti_{0.34}Al_{0.66}N$/TiN multilayers deposited with drum rotation of (b) 1 rpm, (c) 2 rpm, and (d) 4 rpm.

+1, at 41.99°2θ and 43.86°2θ. Appearances of SL effects are present also for the (111) TiN and $Ti_{0.34}Al_{0.66}N$ lattice planes but peak overlapping from the substrate hinders the interpretation. The diffractograms obtained from the 4 rpm multilayer heat treated at 900 °C still show sign of a SL effect but also appearance of *c*-AlN at 44.02°2θ and 37.83°2θ. After heat treatments at 1000 °C the original SL peak seen in as-deposited state has shifted toward the position of (200) TiN. At this temperature also (1010) *h*-AlN are seen at 33.32°2θ. Heat treatments at 1100 °C result in further shift toward the position of the (200) TiN and, as in the case of 1 and 2 rpm multilayers, growth of the (1010) *h*-AlN peak.

Figure 3 shows a STEM micrograph of as-deposited multilayer deposited with a drum rotation of 1 rpm. The micrograph displays alternating dark and bright layers intersecting a dense growth of 200–500 nm wide columns. The columnar growth is consistent with previous observations of arc evaporated monolithic $Ti_{0.34}Al_{0.66}N$.[4] The STEM micrograph in Fig. 4(a) shows homogenous layers with sharp interfaces of the as-deposited 1 rpm multilayer. The darker 25 nm layer corresponds to $Ti_{0.34}Al_{0.66}N$ and the brighter 50 nm layer to the TiN.[6] Figure 4(b) shows the same multilayer (1 rpm) after heat treatment at 900 °C for 2 h. The $Ti_{0.34}Al_{0.66}N$ layer has decomposed to areas of higher Al content surrounded by areas of lower Ti content.[6]

Figure 4(c) shows a cross sectional STEM of as-deposited multilayer deposited with 4 rpm of the drum resulting in $Ti_{0.34}Al_{0.66}N$ and TiN thicknesses of 6 nm and 12 nm, respectively. This multilayer also shows homogenous layers with sharp interfaces. Also here the original $Ti_{0.34}Al_{0.66}N$ layers decompose to areas of higher Al content surrounded by areas of higher Ti content when heat treated at 900 °C [Fig. 4(d)].[6] The main difference from the 1 rpm

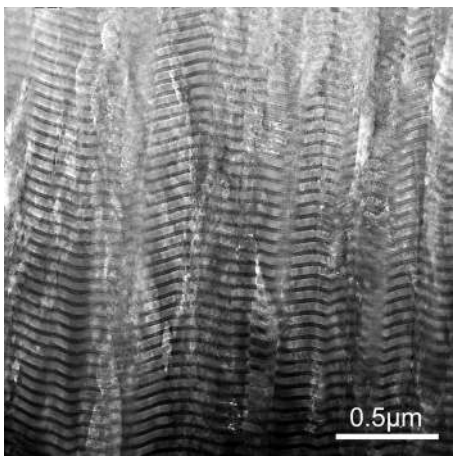

FIG. 3. Overview STEM micrograph of the 1 rpm multilayer in its as-deposited state.

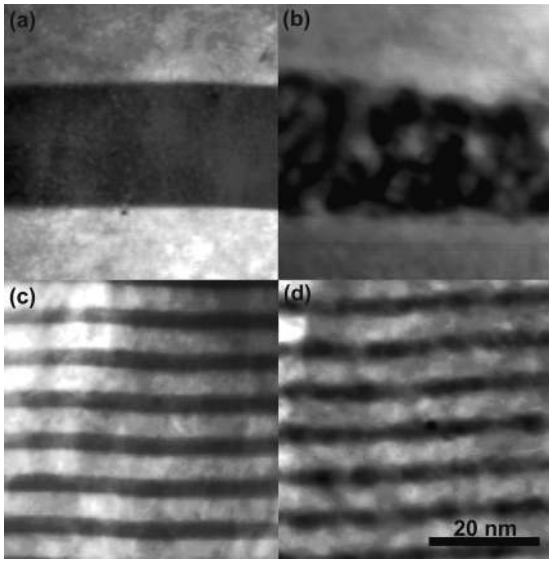

FIG. 4. STEM micrograph of multilayers deposited with drum rotation (a) and (b) 1 rpm and (c) and (d) 4 rpm in (a), (c) as-deposited state and (b), (d)heat treated at 900 °C for 2 h.

multilayer is that the Al rich areas are approximately three times smaller. The 2 rpm multilayer shows the same features as the 4 rpm except that the $Ti_{0.34}Al_{0.66}N$ and TiN have a layer thickness of 12 nm and 25 nm, respectively.

Figure 5 shows a STEM micrograph after heat treatment at 1100 °C of the 1 rpm multilayer. Now, the Al rich areas are larger than the original $Ti_{0.34}Al_{0.66}N$ layers.

Figures 6(a) and 6(b) show high resolution TEM micrographs of a 1 rpm multilayer interface, in its as-deposited and heat treated at 900 °C states, respectively. Lattice coherency within the layer and across layer interface was observed in both states. Same coherency was observed also in the multilayers with faster rotation, 2 and 4 rpm (not shown).

B. Differential scanning calorimetry

Figure 7 shows the heat flow responses of monolithic $Ti_{0.34}Al_{0.66}N$ and 1, 2, and 4 rpm multilayers. All graphs were found to have the same basic appearance with five overlapping exothermic peaks. The five peaks are positioned

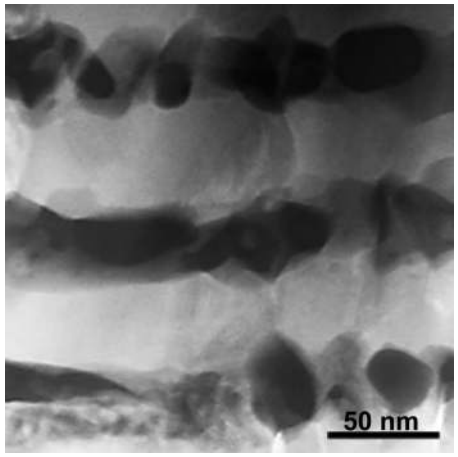

FIG. 5. STEM image of the 1 rpm multilayer heat treated at 1100 °C for 2 h.

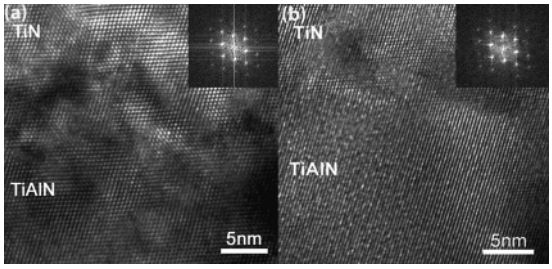

FIG. 6. HR-TEM image and corresponding Fourier transformation of the 1 rpm multilayer interface in (a) as-deposited state and (b) heat treated at 900 °C.

at $T_1 \sim 400$ °C, $700 \leq T_2 \leq 742$ °C, $860 \leq T_3 \leq 960$ °C, $1097 \leq T_4 \leq 1187$ °C, and $1250 \leq T_5 \leq 1280$ °C. The multilayers show an overall decreasing heat flow with deceased multilayer period. The monolithic coating shows distinct peaks while the multilayer thermograms display broader overlapping peaks. A distinct difference between the monolithic coating and the multilayer is seen for peak T_4 where the multilayer peaks are shifted to a higher temperature with 90 °C. Among the multilayers, the T_4 peak is slightly shifted toward higher temperatures with decreasing layer thickness. There is also a difference for the peak T_3 location where the multilayer peaks appears at a temperature up to 100 °C lower than for the monolithic coating. The location of peaks T_1 and T_2 peaks appear to be the same for both multilayers and the monolithic coating and they both appear in a narrow interval of only ~8 °C for all the coatings. The peak T_5 is an oxidation at high temperature caused by small amounts of oxygen present in the protective He-flow.

C. Hardness changes due to isothermal annealing

Figure 8 shows the *ex situ* hardness results of as deposited and isothermally heat treated samples of monolithic TiN and $Ti_{0.34}Al_{0.66}N$ and the multilayer coatings. All Al-containing coatings show the same basic appearance with an almost constant hardness up to 800 °C followed by an increase in hardness (age hardening)[3,4] and a decrease at high temperatures. The monolithic TiN in this work shows an

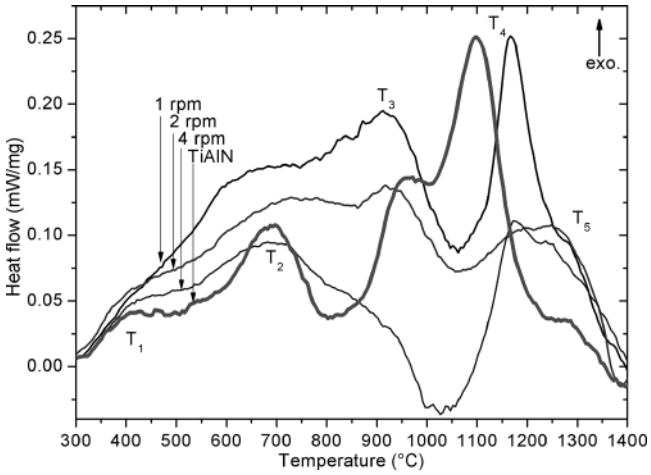

FIG. 7. Differential scanning calorimetry measurements of the multilayered and monolithic coatings.

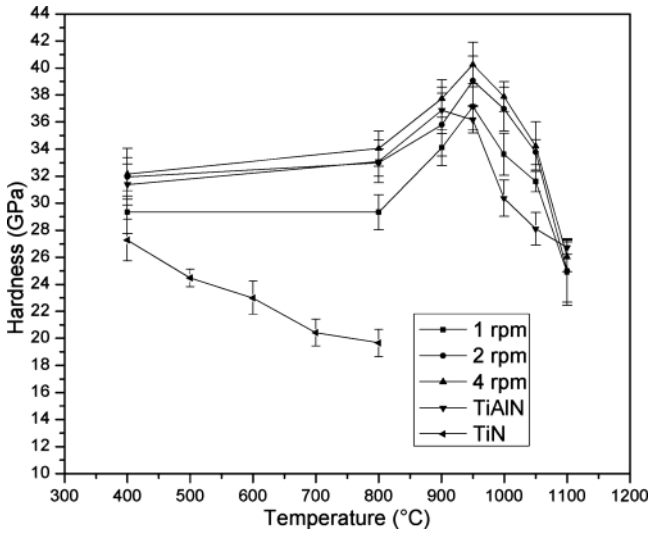

FIG. 8. Hardness values of the as-deposited and heat treated multilayered and monolithic coatings.

overall decrease in hardness with increased annealing temperature which is in accord with earlier observations.[16] The multilayers show an overall increase in hardness with decreased multilayer period. This effect is more pronounced in their heat treated states up 1050 °C. In the as-deposited state the 2 and 4 rpm multilayer coatings show comparable hardness to the monolithic $Ti_{0.34}Al_{0.66}N$ coating while the 1 rpm multilayer is 2.6 GPa softer. This is valid also at 800 °C. At 900 °C the 4 rpm multilayer shows higher hardness compared to the monolithic $Ti_{0.34}Al_{0.66}N$. At 950 °C the hardness of the monolithic $Ti_{0.34}Al_{0.66}N$ is decreasing while all multilayers still show an increase, i.e., all multilayers show a higher hardness than the monolith. The maximum hardness of 40.2 ± 1.6 GPa for the 4 rpm multilayer is achieved after the 950 °C anneal which should be compared to 36.2 ± 1 GPa for the monolithic coating after the same heat treatment. At heat treatments over 950 °C the hardness of all multilayers decreases, however to a lesser degree than the monolithic $Ti_{0.34}Al_{0.66}N$. Heat treatments above 1000 °C results in a substantial decrease in hardness for all coatings and at 1100 °C both the monolithic $Ti_{0.34}Al_{0.66}N$ and the multilayers have a hardness of 26 ± 0.9 GPa.

IV. DISCUSSION

Our results show that deposition of $Ti_{0.34}Al_{0.66}N$ as a multilayer with TiN affects the thermal stability and the mechanical properties compared to a monolithic $Ti_{0.34}Al_{0.66}N$ coating. Hence, we have chosen to first discuss the effect of the multilayer structure on the thermal stability and then how it influences the mechanical properties.

A. Influence of multilayer period on the thermal decomposition

All coatings, multilayers and monolithic, show enthalpy responses including five distinct exothermic peaks. We suggest that the peak labeled T_1 in Fig. 6 corresponds to recovery processes of lattice point defects induced under deposition. This has been inferred also in previous works[17] and is expected at temperatures higher than the deposition temperature of 400 °C. The peak T_2, located between 700 and 750 °C for all coatings has previously been interpreted together with T_3 as an effect of the spinodal decomposition.[18] This is, however, unlikely since spinodal decomposition is a concurrent diffusion process of the constituents and the XRD data in Fig. 2 and *in situ* small angle x-ray scattering data[7] show no evidence for decomposition products at this low temperatures. Hence, we expect T_1 and T_2 to be related to annihilation of defect complexes with different activation energies. Instead the peak labeled T_3 is related to the isostructural decomposition in the *c*-$Ti_{0.34}Al_{0.66}N$ layers and it occurs in the 800–1000 °C regime. This is supported by the occurrence of *c*-TiN and *c*-AlN phases in XRD results of Fig. 2, and the STEM and HRTEM micrographs [Figs. 4(b), 4(d), and 6(b)] which show a compositional modulation of Ti and Al in a coherent cubic lattice after heat treatment to 900 °C. The peak T_4 located in the 1097–1187 °C regime corresponds to the *c*-AlN to *h*-AlN transformation. This is the final step of decomposition and the original *c*-$Ti_{0.34}Al_{0.66}N$ will past this step consist of *c*-TiN and *h*-AlN which is in accord with XRD and STEM data in Figs. 2(a)–2(d) and 5.

The DSC data from the multilayers indicate that the formation of *h*-AlN is suppressed in the multilayers compared to the monolithic coating. This is also supported by the diffractograms in Figs. 2(b) and 2(c) where the intensity from the *h*-AlN is increasing between 1000 and 1100 °C while it is constant for monolithic coating [Fig. 2(a)]. The T_4 peak is shifted from 1097 °C for the monolithic coating to 1187 °C for the 4 rpm multilayer, i.e., a suppression of the decomposition by 90 °C. We suggest that the higher decomposition temperature of all multilayers is an effect of coherency strain introduced by the presence of TiN-layers which has previously been suggested theoretically to influence the spinodal decomposition.[19] The coherency across the multilayer interfaces introduces a compressive strain in the $Ti_{0.34}Al_{0.66}N$ layers. Based on the lattice mismatch for cube on cube growth of $Ti_{0.34}Al_{0.66}N$ on TiN suggests a stress of ≈4.3 GPa (*c*-AlN=4.12, *c*-TiN 4.24 and *c*-TiAlN=4.17 Å).[20] Large compressive stresses have recently been shown to suppress the *c*-AlN to *h*-AlN transformation.[21] Moreover, the shape of the precipitates in Figs. 4(d) and 5 suggests that their growth is limited across layer interfaces. It has theoretically been shown that if precipitates are smaller than the critical radius r_{crit}, the coherent state gives the lowest total energy, while it is more favorable for large precipitates ($>r_{crit}$) to be incoherent.[22] As a result the growth of the *c*-AlN domains is suppressed when confined in the multilayers such that r_{crit} is reached at a higher temperature. Consequently, the higher transformation temperature results in a higher T_4 peak location for the multilayers compared to the monolith as seen in Fig. 7. The restricted growth of the AlN precipitates due to the immiscibility of AlN in TiN and the associated shape change in the precipitates also implicate longer diffusion paths compared to spherical precipitation growth.[22] This will contribute to a slower decomposition rate of $Ti_{0.34}Al_{0.66}N$ and that it occurs over a wider temperature range. Indirect evidence of this is seen if Fig. 7 where the multilayers show a broader T_3 peak compared to the monolithic coating. In

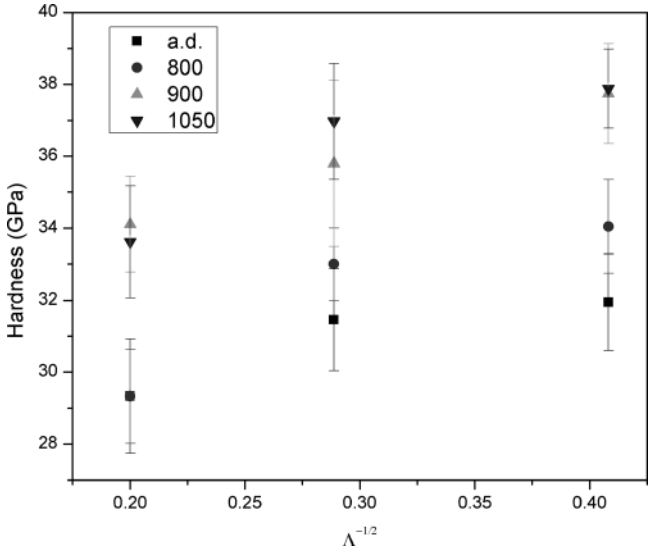

FIG. 9. Hardness of as-deposited and heat treated $Ti_{0.34}Al_{0.66}N/TiN$ multilayer coatings plotted vs $\Lambda^{-1/2}$.

addition, the onset of spinodal decomposition, peak T_3, occurs at slightly lower temperatures for the multilayers. Also here the largest difference, 100 °C, is seen when comparing the monolithic coating with the 4 rpm multilayer. This is again in accord with the prediction that the enthalpy of mixing is increasing for a strained solid solution of TiAlN.[21]

B. Influence of multilayer period and heat treatments on the hardness

Annealing monolithic TiN results in a decrease in hardness toward its intrinsic hardness of approximately 20 GPa (Refs. 23 and 24) due to defect annhiliation.[25] A similar defect annihilation occurs in the multilayers (cf. DSC-peaks T_1 and T_2 in Fig. 7). However, the hardness of the multilayers stays constant or increase slightly at a level comparable or higher than monolithic, $Ti_{0.34}Al_{0.66}N$ after being annealed at 800 °C despite containing 60 vol % TiN. The reason for this effect is multilayer hardening,[11] which has been observed for many other transition metal nitride systems with elastic shear modulus differences.[26,27] The multilayers in this study show a XRD response consistent with local epitaxial growth of a fully coherent SL that results in SL satellites.[28] Hence the requirements for multilayer hardening are fulfilled. The 1 rpm multilayer, which has the longest period $\Lambda = 25 + 50$ nm, exhibits a lower hardness compared to the other two multilayers which is expected due to longer dislocation pile-ups and a less efficient multilayer hardening.[11]

All Al-containing coatings exhibit age hardening when annealed above 800 °C. Strain fields as a result of the coherency and molar volume difference between *c*-TiN and *c*-AlN effectively hinder dislocation motions and increase the hardness.[3,4] Hence, a combination of multilayer and Orowan hardening is suggested as the underlying mechanisms of the higher hardness.[29–31] A clear indication that this results in a Hall–Petch type dependency is presented in Fig. 9 where the hardness versus the layer period shows a negative linear relationship, similar to what has been reported for other multilayered thin films.[32]

The monolithic $Ti_{0.34}Al_{0.66}N$ shows a drastic decrease in hardness at 950 °C which is related to the decomposition of metastable *c*-AlN into stable *h*-AlN. The transformation is accompanied by a ~20% unit cell volume increase and a loss of the coherency and thus increase the possibility of dislocations movments.[33–35] Since this transformation is evidently suppressed to higher temperatures in the multilayers the decrease in hardness is seen at higher annealing temperatures.

V. CONCLUSIONS

Monolithic and nanolaminated multilayer coatings consisting of TiN and $Ti_{0.34}Al_{0.66}N$ with different layer periods have been synthesized by reactive arc evaporation and subjected to postdeposition high temperature anneals. We present evidence of an improved thermal stability of the $Ti_{0.34}Al_{0.66}N$ in a multilayer structure compared to a monolithic $Ti_{0.34}Al_{0.66}N$ coating. Our DSC results show that the first step of the decomposition is shifted to lower temperatures while the second step is shifted to higher temperatures. High resolution TEM micrographs show coherency over the multilayer interfaces both in as-deposited and 900 °C annealed state. STEM imaging reveals that the shape and size of the *c*-AlN precipitates are affected by the multilayer period. We propose that both the first and second step of decomposition is affected by the introduced coherency stresses in the TiAlN layer. Moreover, as a result of the change in thermal stability, the multilayers show retained hardness compared to the monolithic $Ti_{0.34}Al_{0.66}N$ coating at elevated temperature. We conclude that internal architecture can be used to control thermal evolution of the material.

ACKNOWLEDGMENTS

The financial support from the Swedish Research Council (VR) and the Swedish Foundation for Strategic Research (SSF) is gratefully acknowledged. We also acknowledge Kent Johansson at Seco Tools AB for performing the heat treatments.

[1] O. Knotek, M. Böhmer, and T. Leyendecker, J. Vac. Sci. Technol. A **4**, 2695 (1986).
[2] H. A. Jehn, S. Hofmann, V.-E. Rückborn, and W.-D. Münz, J. Vac. Sci. Technol. A **4**, 2701 (1986).
[3] A. Hörling, L. Hultman, M. Odén, J. Sjölén, and L. Karlsson, J. Vac. Sci. Technol. A **20**, 1815 (2002).
[4] A. Hörling, L. Hultman, M. Odén, J. Sjölén, and L. Karlsson, Surf. Coat. Technol. **191**, 384 (2005).
[5] M. Odén, J. Almer, G. Håkansson, and M. Olsson, Thin Solid Films **377–378**, 407 (2000).
[6] A. Knutsson, M. P. Johansson, P. O. A. Persson, L. Hultman, and M. Odén, Appl. Phys. Lett. **93**, 143110 (2008).
[7] M. Odén, L. Rogström, A. Knutsson, M. R. Terner, P. Hedström, J. Almer, and J. Ilavsky, Appl. Phys. Lett. **94**, 053114 (2009).
[8] P. H. Mayrhofer, D. Music, and J. M. Schneider, Appl. Phys. Lett. **88**, 071922 (2006).
[9] B. Alling, A. V. Ruban, A. Karimi, O. E. Peil, S. I. Simak, L. Hultman, and I. A. Abrikosov, Phys. Rev. B **75**, 045123 (2007).
[10] L. Hultman, C. Engstrom, and M. Odén, Surf. Coat. Technol. **133–134**, 227 (2000).
[11] J. S. Koehler, Phys. Rev. B **2**, 547 (1970).
[12] A. F. Jankowski and T. Tsakalakos, J. Phys. F: Met. Phys. **15**, 1279 (1985).
[13] E. O. Hall, Proc. Phys. Soc. B **64**, 747 (1951).
[14] N. J. Petch, J. Iron Steel Inst. **174**, 25 (1953).

[15]W. C. Oliver and G. M. Pharr, J. Mater. Res. **7**, 1564 (1992).
[16]L. Karlsson, A. Hörling, M. P. Johansson, L. Hultman, and G. Ramanath, Acta Mater. **50**, 5103 (2002).
[17]J. Almer, M. Odén, and G. Håkansson, Thin Solid Films **385**, 190 (2001).
[18]P. H. Mayrhofer, A. Hörling, L. Karlsson, J. Sjölen, C. Mitterer, and L. Hultman, Appl. Phys. Lett. **83**, 2049 (2003).
[19]D. J. Seol, S. Y. Hu, Y. Hu, Y. L. Li, J. Shen, K. H. Oh, and L. Q. Chen, Acta Mater. **51**, 5173 (2003).
[20]Powder Diffraction File, JCPS International Center for Diffraction Data, Swarthmore, PA, 1992; TiN (38-1420), AlN (25-1495).
[21]B. Alling, M. Odén, L. Hultman, and I. A. Abrikosov, Appl. Phys. Lett. **95**, 181906 (2009).
[22]D. A. Porter and K. E. Easterling, *Phase Transformation in Metals and Alloys*, 2nd ed. (Stanley Thornes, Cheltenham, 1992).
[23]H. Ljungcrantz, M. Odén, L. Hultman, J. E. Greene, and J. E. Sundgren, J. Appl. Phys. **80**, 6725 (1996).
[24]M. Odén, H. Ljungcrantz, and L. Hultman, J. Mater. Res. **12**, 2134 (1997).
[25]M. Odén, J. Almer, and G. Håkansson, Surf. Coat. Technol. **120–121**, 272 (1999).
[26]X. Chu and S. A. Barnett, J. Appl. Phys. **77**, 4403 (1995).
[27]M. Shinn, L. Hultman, and S. A. Barnett, J. Mater. Res. **7**, 901 (1992).
[28]B. K. Agarvall, *X-ray spectroscopy—An introduction* (Springer-Verlag, Berlin, 1979).
[29]J. D. Embury and J. P. Hirth, Acta Metall. **42**, 2051 (1994).
[30]A. Misra, M. Verdier, Y. C. Lu, H. Kung, T. E. Mitchell, M. A. Nastasi, and J. D. Embury, Scr. Mater. **39**, 555 (1998).
[31]Y. C. Lu, H. Kung, A. J. Griffin, M. A. Nastasi, and T. E. Mitchell, J. Mater. Res. **12**, 1939 (1997).
[32]H. Söderberg, M. Odén, J. M. Molina-Aldareguia, and L. Hultman, J. Appl. Phys. **97**, 114327 (2005).
[33]N. E. Christensen and I. Gorczyca, Phys. Rev. B **47**, 4307 (1993).
[34]M. Ueno, A. Onodera, O. Shimomura, and K. Takemura, Phys. Rev. B **45**, 10123 (1992).
[35]Q. Xia, H. Xia, and A. L. Ruoff, J. Appl. Phys. **73**, 8198 (1993).